Understanding Local Defects in Li-ion Battery Electrodes through Combined DFT/NMR Studies: Application to $LiVPO_4F$

T. Bamine[a,b], E. Boivin[a,b,f], F. Boucher[c], R. J. Messinger[b,d,e], E. Salager[b,d], M. Deschamps[b,d], C. Masquelier[b,f], L. Croguennec[a,b], M. Ménétrier[a,b] and D. Carlier[a,b*]

[a] *CNRS, Univ. Bordeaux, Bordeaux INP, ICMCB UPR 9048, F-33600 Pessac, France*

[b] *RS2E, Réseau Français sur le Stockage Electrochimique de l'Energie, FR CNRS 3459, F-80039 Amiens Cedex 1, France*

[c] *Institut des Matériaux Jean Rouxel (IMN), Université de Nantes, CNRS, 44322 Nantes, France*

[d] *CNRS, CEMHTI, UPR 3079, Université d'Orléans, Orléans, France*

[e] *Department of Chemical Engineering, The City College of New York, CUNY, New York, NY 10031 USA*

[f] *Laboratoire de Réactivité et de Chimie des Solides, CNRS-UMR#7314, Université de Picardie Jules Verne, F-80039 Amiens Cedex 1, France*

Abstract

In a recent study, we showed by solid-state NMR that $LiVPO_4F$, which is a promising material as positive electrode for Li-ion batteries, often exhibits some defects that may affect its electrochemical behavior. In this paper, we use DFT calculations based on the projector augmented-wave (PAW) method in order to model possible defects in this (paramagnetic) material and to compute the Fermi contact shifts expected for Li nuclei located in their proximity. The advantage of the PAW approach versus FP-LAPW we have been previously using is that it allows considering large supercells suitable to model a diluted defect. In the first part of this paper, we aim to validate the Fermi contact shifts calculation using the PAW

approach within the VASP code. Then we apply this strategy for modeling possible defects in $LiVPO_4F$. By analogy with the already existing homeotypic $LiVOPO_4$ phase, we first replace one fluoride ion, along the VO_2F_4chains, by an oxygen one and consider, in a second step, an association with a lithium vacancy. As a result, the agreement between the calculated NMR spectra and the experimental one is satisfying. In both cases, the local electronic structure and the spin transfer mechanisms from V^{3+} or V^{4+} ions to the Li nuclei are analyzed.

*Corresponding author (D. Carlier): dany.carlier@icmcb.cnrs.fr

Introduction

In the past few years, Li-ion batteries have been used extensively for energy storage in portable electronics. In order to widely apply this technology to other applications as large-scale stationary storage or transportation, their energy and power density, cost, safety, and cycle lifetime have to be improved. For this purpose, much interest has been addressed to new materials that could replace commercially available ones. Especially, several polyanionic materials have been investigated[1].

It appears that the knowledge of the local structure in positive electrode materials is crucial for the understanding of their electrochemical properties. Indeed, some materials may exhibit local disorder or heterogeneities such as defects, amorphous components, or domains of varying stoichiometry, all of which may affect their electrochemical energy storage properties. Complementarily to X-ray diffraction studies, which yield long-range structural information, solid-state ^{7}Li nuclear magnetic resonance (NMR) spectroscopy is a powerful probe to characterize lithium local environment in these systems.

As most of the positive electrode materials are paramagnetic, their NMR spectra are consequently dominated by the hyperfine interactions between nuclear and electron spins. Using Magic Angle Spinning (MAS) NMR, the shifts are dominated by the Fermi contact term (due to the interaction between the nuclear spin and the surrounding unpaired electron spins), that can be expressed as:

$$\delta_{iso}^{i}(T) = \frac{1}{3SN_A}\rho^{i}(0)\chi_M(T) \qquad \text{eq. (1)}$$

where S is the spin quantum number of the paramagnetic ion, $\rho^{i}(0)$ is the computed spin density on the *i* nucleus and χ_M the molar magnetic susceptibility (at the temperature of the NMR measurement).

The interpretation of Fermi contact shift interactions can be done via the analysis of local geometries and their suitability for electron spin transfers based either on delocalization or polarization-type mechanisms leading to positive or negative shifts, respectively[2]. This effort is greatly supported by calculation strategies. For several years, we have been using DFT calculations that are well suited for the study of periodic inorganic materials, with two main objectives:

i) assign the different ^{7}Li MAS NMR signals

ii) understand the spin transfer mechanisms from the magnetic transition metal ions to the Li nucleus.

The combined NMR/DFT approach therefore allows discussing the chemical bonds in different materials from a solid-state chemistry perspective. After our initial work on various oxides, which introduce a qualitative approach based on plane waves and pseudopotential calculations (VASP code)[2,3], we recently developed a more quantitative one. We used an all-electron and full potential method (WIEN2k code) together with the experimental susceptibilities in order to closely reproduce the experimental Fermi contact shift[4]. Moreover, we also improved the analysis of these shifts, by making the link with the chemical bonds in the materials, using spin DOS and 3D spin density maps in selected energy domains[3]. Recently a few other groups also developed similar approaches to compute the Fermi contact shifts, but with different methods: i) Mali *et al.* for Li_2MnSiO_4 polymorphs with the "GIPAW" package of the Quantum Espresso code to compute the spin density at the Li nucleus and a Curie model for the magnetic susceptibility[5]. ii) Grey and co-workers for several phosphate and oxides phases with an all-electron LCAO code, namely Crystal06 with B3LYP hybrid exchange-correlation functionals to compute the electron spin density at the Li nucleus and a scaling factor using experimentally determined parameters to model the magnetic susceptibility at the measurement temperature[6,7].

In this paper, we aim to address the problem of modeling a diluted defect in a paramagnetic material. In order to consider large supercells, the use of the VASP code (plane waves and PAW potentials) is preferred to that of the more computer-demanding "all-electron" WIEN2k (FP-FLAPW) code. Indeed, the computation of the spin density at the nuclei is now available in the latest versions of VASP (> 5.3). However, as no study of Fermi contact shift calculations using this code is yet available in the literature, we aim, in a first step, to validate such calculations and test different PAW potentials for several polyanionic battery materials. Our results are compared with those of WIEN2k either calculated previously[3,4,8,9] or obtained in the present paper. In a second step, we used such calculations to interpret the NMR signals linked to the presence of a defect in $LiVPO_4F$, a promising candidate for positive electrode material for Li-ion batteries. This compound exhibits a Tavorite-type structure. While X-ray and neutron diffraction analysis did not detect any impurity in this compound, the ^{7}Li MAS NMR spectrum shows extra peaks that cannot be interpreted simply. The first ^{7}Li MAS NMR study of $LiVPO_4F$ was reported by Goward *et al.*[10] but they did not provide any explanation of these additional signatures. Kosova *et al.*[11] suggested more recently that these extra signals

would correspond to the three Li sites of the anti-Nasicon $Li_3V_2(PO_4)_3$, which could be present as impurity, even though their positions do not match exactly those reported in other studies[3,12]. In fact, recently[13], using 2D ^{7}Li NMR experiments, we could show that the additional signals correspond to Li sites close to structural and/or chemical defects in $LiVPO_4F$, and not to Li in impurity phases as suggested previously[11]. We thus considered several structural and chemical hypotheses for modeling the defects in $LiVPO_4F$ and compared the resulting calculated Fermi contact shifts with the experimental ones. Moreover, we analyzed the spin transfer mechanisms from the vanadium ions to the Li nuclei and discussed them in relation with the electronic structure of the material.

Experimental

$LiVPO_4F$ samples were prepared using a two-step solid-state synthesis described in details in reference[14]. This synthesis first involves the formation, by a carbothermal route, of an intermediate precursor: a carbon-coated VPO_4. The quantity of carbon was then determined by thermogravimetric analyses in order to perfectly control the preparation of a (1:1) stoichiometric mixture of LiF and VPO_4. The pure $LiVPO_4F$ material is then obtained in a second step through a thermal treatment under argon at high temperature.

^{7}Li MAS NMR spectra were recorded on a Bruker Avance III spectrometer with a 7 T magnet (116 MHz resonance frequency for ^{7}Li). A standard Bruker 2.5 mm MAS probe at a 30 kHz typical spinning speed was used. A Hahn echo sequence was used with a 90° pulse of 1.2 µs. The 0 ppm external reference used was a 1M LiCl aqueous solution.

First principles calculations were performed within the Density Functional Theory (DFT) framework. Calculations using PAW potentials were performed with the Vienna ab initio Simulation Package (VASP) code[15]. A plane wave energy cut-off of 600 eV and a k-mesh dense enough to reach convergence were used. Note that different PAW-PBE potentials implemented in the VASP code were tested. The best agreements were obtained using the standard PAW-PBE potentials for O, P, and V and the "sv" PAW-PBE potential for Li that treats the 1s shell as valence states. All calculations were spin polarized type with a ferromagnetic type ordering which is considered appropriate for the Fermi contact shift, as described in reference[2]. In the Generalized Gradient Approximation (GGA), the inherent self-

interaction error has detrimental effect on localized transition-metal d (or rare earth f) orbitals. Thus, the GGA is not well appropriate for describing these orbitals but many methods have been proposed to overcome this deficiency. In our calculations, we have used the "GGA+U" approach, where Hubbard type interaction is added to localize d (or f) electrons, with the following U_{eff} (U-J) values: 4.9 eV for Fe, 3.5 or 4.5 eV for V, and 5 eV for Mn. Another approach that is now widely used to remove the self-interaction error[16] is based on hybrid functionals: a portion of Fock-type exact exchange is introduced to replace part of the GGA exchange potential. However, the hyperfine coupling constants calculation is not yet supported in VASP when hybrid functionals are used. Partial charges on V ions were determined using a Bader charge analysis. The implementation of this method to the VASP output is described in references [17–19]

For the Fermi contact shifts calculations, the VASP code is providing the hyperfine coupling constant taking into account valence and core contribution:

$$A_{iso} = \frac{2}{3}\frac{\mu_0 \gamma_e \gamma_N}{<S_z>}\int \delta_T(r)\rho_s(r+R_I)dr \qquad \text{(eq. 2)}$$

where ρ_s is the population difference at the nucleus between the spin-up and the spin-down energy levels, that we will denote as "electronic spin density", μ_0 is the magnetic susceptibility of free space, γ_e the electron gyromagnetic ratio, γ_N the nuclear gyromagnetic ratio of the nucleus, R_I the nucleus radius, and $\langle S_Z \rangle$ the expectation value of the z-component of the total electronic spin. $\delta_T(R)$ is a smeared out δ function, as described in the appendix of reference[20]. Therefore the Fermi contact shift was further determined using equations 1 and 3:

$$\rho^i(0) = \frac{A_{iso}.S(tot)}{\gamma_N} \qquad \text{eq. (3)}$$

where $S(tot)$ is the total magnetic moment in the cell, γ_N the nuclear gyromagnetic ratio of the nucleus, and A_{iso} the hyperfine coupling constant.

With the following gyromagnetic ratio ($MHz.T^{-1}$): Li: 16.546, V: 11.213, Fe: 1.38, Mn: 10.56, P: 17.235, O: 5.772, H: 42.576, F: 1.76. The molar magnetic susceptibility was taken from experimental data using a Curie-Weiss law with C ($emu.K.mol^{-1}$) equal to 3.64, 1.01, 2.66, 2.73, 0.87 and 0.35, and θ(K) equal to -55, -37, -57, -11.7, -36 and -20, respectively for $Li_3V_2(PO_4)_3$[3], $Li_3Fe_2(PO_4)_3$[3], $LiFePO_4.OH$[8], $LiMnPO_4.OH$[8], $LiVPO_4F$[14], and $LiVOPO_4$[21]. The

temperature T was chosen equal to 320K, which corresponds approximately to the temperature reached in the rotor during a 30 kHz magic angle spinning experiment[3].

All-electron/Full-potential Linearized Augmented Plane Wave (FP-LAPW) calculations were performed using the WIEN2k package, as described in detail in references[3,4,8,9]. 3D calculated spin density maps were plotted using the VESTA software (Visualization for Electronic and Structural Analysis)[22].

Results and discussion

We aim, in a first part, to validate the Fermi contact shifts calculations using the VASP code and thus to test the different available potentials for different polyanionic phases : i) with the Tavorite structure (Li*M*PO_4.OH with *M* = Mn, Fe, *M*$PO_4.H_2O$ with *M* = V, Mn, Fe and ideal $LiVPO_4F$), ii) with the anti-Nasicon structure ($Li_3M_2(PO_4)_3$ with *M* = V, Fe), and iii) with the olivine structure (Li*M*PO_4 with *M* = Mn, Fe, Co, Ni) . The Fermi contact shifts calculations were done for the ^{7}Li, ^{19}F, ^{1}H, and ^{31}P nuclei with the VASP code and compared with those obtained with the WIEN2k one, either previously or in this study.

Figure 1 shows the calculated shifts obtained for ^{7}Li in the Tavorite (**Figure 1a**) and anti-Nasicon (**Figure 1b**) materials with the PAW and FP-LAPW methods, and compared with the experimental ones. Results obtained for the other nuclei and for the olivine materials are given and discussed in the supplementary information (**Figures S1a-c**). The Tavorite-type materials (except $LiVOPO_4$) and the olivine-type ones exhibit all a single Li site, whereas the anti-Nasicon type materials exhibit three sites. First of all, whatever the method used (GGA or GGA+U with PAW or FP-LAPW approaches) the sign of the calculated shifts and the relative order of magnitude are well reproduced for all compounds. For the Mn and Fe compounds, a better agreement with the experimental shifts is obtained using GGA+U calculations with PAW and FP-LAPW methods as expected by a stronger localization of the d electrons on the transition metal. Even if the calculated shifts are always larger than the experimental ones, the best agreement is clearly obtained for the FP-LAPW method (WIEN2k code) that better treats the core electrons than the PAW one (VASP code). For the vanadium-containing compounds, however, all calculations yield to a fairly good agreement with the experimental shifts. This difference in behavior can come from the electronic configuration of V^{3+} ions in octahedral sites (t_{2g}^2, e_g^0), that only exhibits two unpaired t_{2g} electrons, whereas Mn^{3+} (t_{2g}^3, e_g^1), and Fe^{3+}

(t_{2g}^3, e_g^2) do exhibit also unpaired e_g electrons. These latter electronic configurations may strongly polarize deeper doubly occupied core levels that are better treated within the FP-LAPW than with the PAW approach. Nevertheless, these results allowed us to validate our new approach using PAW potential to model defects in electrode materials. Especially for V-containing compounds, we expect a rather good agreement between the experimental and calculated shifts. In the following we will focus on the $LiVPO_4F$ material, a very promising positive electrode material for the next generation of Lithium-ion batteries.

$LiVPO_4F$ exhibits a Tavorite-type structure described in **Figure 2**: VO_4F_2 octahedra share fluorine atoms, forming chains connected to each other via PO_4 tetrahedra (**Figure 2a**). The V^{3+} ions are located in two octahedral sites V1 and V2 with a very narrow range of V−O distances between 1.96 and 1.99 Å. The V−F distances along the chains are very similar around 1.98 Å (**Figure 2b**)[14]. The ^{7}Li MAS-NMR spectrum (**Figure 3**) of $LiVPO_4F$ shows several signals in addition to the main one (116 ppm) which corresponds to a well identified single Li site in this material, LiO_4F (**Figure 2c)**[10,13]. In the following, we will first interpret the main signal located at 116 ppm for the Li site in $LiVPO_4F$ based on calculated 3D spin density maps. Then, we will aim at modeling the possible local defects in this material.

Spin transfer mechanisms in ideal $LiVPO_4F$

Table 1 summarizes the ^{7}Li Fermi contact shifts calculated for the ideal $LiVPO_4F$ compound using the PAW method and GGA or GGA+U with different U values. The 130 ppm value computed with GGA is already really close to the experimental one (116 ppm). Adding a U value for the calculation localizes more the 3d electrons on the V ions and therefore decreases the amount of transferred electronic spin on the adjacent Li. However, the result is not very sensitive to values chosen for the Hubbard term as resulting values are quite similar (in the 110-121 ppm range). In the following of this paper, GGA and GGA+U with U = 3.5 eV for 3d electrons of V^{3+} will be reported. Note that calculations performed with U = 4.5 eV do not modify qualitatively the spin transfer mechanisms but change globally the calculated shifts magnitude as a larger U localizes more the d electrons on V. In the paper, we present the results obtained for U = 3.5 eV as the agreement between calculated and experimental shifts was better.

The optimized geometries compared to the experimental one are provided in the supplementary information (**Table S2**).

In order to understand the electronic spin transfer mechanism from the V^{3+} ions to Li in the ideal structure of $LiVPO_4F$, we plotted calculated 3D spin density map in selected regions of the cell. In **Figure 4a**, the maximum spin density is observed in a region around the two V sites that come from two occupied orbitals having a t_{2g} shape, *i.e.* with orbital lobes pointing between O/F ligands. Each V thus exhibits a lobe pointing directly toward the Li site through the common edge between the LiO_4F and VO_4F_2 polyhedra. Therefore, the spin transfer mechanism occurring here is a delocalization mechanism by the hybridization between the occupied V t_{2g} and the Li s orbitals as better seen for one V1 ion using a 2D density map and a scheme in **Figure 4b**.

Understanding defects in $LiVPO_4F$

As the ^{7}Li MAS NMR spectrum of $LiVPO_4F$ exhibits extra signals attributed to the presence of defects in the material, we aim to model possible local defects in this material, analyze the structure (after relaxation of the considered supercell) and the local electronic structure around the defect, compute the resulting Li Fermi contact shifts and attempt a correlation between the calculated shifts with the experimental ones, and analyze the spin transfer mechanisms.

Among the different possible defect hypotheses, we first thought of the replacement of a fluoride ion by a hydroxyl group. We however very quickly discarded this hypothesis as the ^{1}H MAS NMR spectrum of this material does not show any presence of hydrogen. Furthermore, this kind of defect would not have impacted the valence state of the vanadium, and so the spin transfer mechanism. The same reason was used for discarding the Li-V anti-site hypothesis. The discarded hypothesis of replacing one fluorine by a hydroxyl is supported by our recent synthesis of the $LiVPO_4.OH$ phase[23] where none of ^{7}Li NMR signal corresponds to one of the defect signals in $LiVPO_4F$.

a) $LiVPO_4F_{0.94}O_{0.06}$

As a hypothetical structure with defects, and by analogy with $LiVOPO_4$ (also a Tavorite type compound[21]), we considered the replacement of a fluoride ion by an oxygen. The resulting

electronic structure is analyzed together with its impact on possibly different Li environments in terms of NMR. In order to model this diluted defect, a large 128 atoms supercell was used (2a x 2b x 2c) leading to the $Li_{16}V_{16}(PO_4)_{16}F_{15}O$ (i.e. $LiVPO_4F_{0.94}O_{0.06}$) formula. According to this formula, one expects the formation of one V^{4+} in the unit cell to equilibrate the negative charge coming from the additional oxygen atom. The structure is also locally modified as two V octahedra share an O corner instead of F. They will be further denoted as V1' and V2'. The structure of the supercell was relaxed testing both the GGA and the GGA+U, and the local electronic structure around the defect was analyzed. However, the GGA does not give the expected result as it leads to the formation of two quasi-equivalent V ions around the O defect in term of V-O, V-F distances and charges, exhibiting an intermediate state between 3+ and 4+. On the other hand, with the GGA+U, among the two V ions surrounding the O defect, only one V seems to be strongly affected by the charge transfer. Thus, only the results coming from the GGA+U calculations will now be considered. **Figure 5** shows the local distances optimized around the O defect in $Li_{16}V_{16}(PO_4)_{16}F_{15}O$. The V2' ions exhibit a short V-O distance (1.72 Å) and a longer opposite V-F one (2.11 Å), whereas the V1' ions exhibit quasi similar V-O and V-F distances (around 2.06 Å). Such a short V-O distance can be explained with the formation of a vanadyl bond as observed in the Tavorite $LiV^{IV}PO_4O$ phase[11]. In the latter phase, short and long V-O distances alternate along the V-O-V-O chains (1.71 Å; 2.21 Å; 1.63 Å; 2.17 Å) due to the formation of vanadyl bonds. The short V-O distance obtained after geometry optimization for $Li_{16}V_{16}(PO_4)_{16}F_{15}O$, is in the same range and tends to indicate that among the two V ions surrounding the O defect, a localized V^{4+} ion has been formed, whereas the other one remains V^{3+}. This was clearly confirmed by analyzing the partial DOS, Bader charges, magnetization in a 0.64 Å radius (ionic radius size for a V^{3+} ions in [6] environment) sphere around V (see **Table S3** and **Table S4** in supplementary information) and spin density maps. **Figure 6** shows the spin density maps calculated in the $Li_{16}V_{16}(PO_4)_{16}F_{15}O$ cell (**Figure 6a**) and locally around the defect (**Figure 6b**). The maximum spin density is clearly located in a single t_{2g} orbital for V2' ion as for $LiVOPO_4$ (also denoted $LiVPO_4O$), and is perpendicular to the V-O short distance direction. This $(d_{xy})^1$ electronic configuration is typical of V^{4+} involved in a vanadyl bond along the z-direction. All other V ions in the $Li_{16}V_{16}(PO_4)_{16}F_{15}O$ cell exhibit standard V-O and V-F distances and maximum spin density in regions involving two t_{2g} orbitals, as observed also for $LiV^{III}PO_4F$. These ions are all in the +III charge state, but do not all exhibit the same local electronic structure in term of t_{2g} mixing. For example, V2'' exhibits a (d_{xy}^0, d_{xz}^1, d_{yz}^1) electronic configuration, with clearly no spin density in the t_{2g} orbital perpendicular to the V-F direction along the chain

denoted as z (**Figure 6a)**. This specific local electronic structure of the V ions will, of course, affect the spin quantity transferred to adjacent Li ions, leading to several Li signals. We could thus classify 4 main different environments for Li in the structure as shown in **Figure 7**. The Fermi contact shifts were calculated for all the Li types and their positions are reported schematically in **Figure 8** below the experimental spectra.

The Li nuclei located in similar environment than the one in ideal $LiVPO_4F$ are denoted by Li_{LVPF}. Those Li undergo similar spin transfer mechanisms as described for $LiVPO_4F$ also slightly differences in the calculated shift values are obtained due to slight differences in Li-O-V distances and angles. Other Li types exhibit difference environments and spin transfer mechanisms as described below. For the Li_a environment, the two V octahedra share an edge with Li_aFO_4 exhibit t_{2g} lobes pointing towards Li_a, but with different shapes (Figure 7a). The V on the left side of **Figure 7a** exhibits a spin density similar to that of the V ions in ideal $LiVPO_4F$. On the opposite, the V on the right side exhibits spin density only in the d_{xy} orbital resulting from the formation of the vanadyl bond as discussed before, and this orbital points directly toward the Li_a position. By delocalization mechanism involving the overlap between these t_{2g} orbitals and the Li_a s one, a positive electronic spin density is transferred to the Li nucleus, larger than for Li in ideal $LiVPO_4F$ leading to a larger Fermi contact shift (**Figure 8)**. **Figure 7b** presents the Li_b environment. Among the two V octahedra sharing an edge with Li_bFO_4, only one exhibits a t_{2g} lobe pointing towards Li_b, since V2'' on the left side of the **Figure** has no spin in the d_{xy} orbital. The delocalization mechanism thus occurs only through one common edge and the calculated shift for Li_b is weaker than the one of Li in ideal $LiVPO_4F$ (**Figure 8**). In turn, Li_c receives spin density from the V1 on the right side of the **Figure** by a delocalization mechanism and no spin density for the V2'' on the left side (**Figure 7c**) ; the resulting calculated shift is thus weaker than the value obtained for Li ideal $LiVPO_4F$ (**Figure 8**). For Li_d, the spin transfer mechanism is really different (**Figure 7d**). Indeed, Li_d is coordinated with the O constituting the defect in the cell. The V2'' on the left side does not exhibit spin density pointing toward Li_d and the O defect on the right side exhibits a strong negative spin density due to the polarization of deeper bonding levels implying V 3d orbitals and O 2p orbitals and also Li 2s orbital. As a result, a negative spin density is calculated on Li_d (**Figure 8**) as the polarization mechanism dominates here.

Among the calculated shifts in the $Li_{16}V_{16}(PO_4)_{16}F_{15}O$ cell, some might explain the experimental ones as we predicted some signals to be more or less shifted than the one of Li environment in $LiVPO_4F$. However, no negative signal was experimentally recorded; only

spinning sidebands are located in this region (this was proved by changing the spinning frequency and the magnetic field). We therefore tested a new structural model obtained by associating the F/O substitution with a lithium removal. So, the Li_d ion is removed from the cell and, doing so, one expects the structure to be more stable, as two V^{4+} might be formed around the O defect. The formula of the considered unit cell is now $Li_{15}V_{16}(PO_4)_{16}F_{15}O$ (i.e. $Li_{0.94}VPO_4F_{0.94}O_{0.06}$).

b) $Li_{0.94}VPO_4F_{0.94}O_{0.06}$

As a second model for the defect, we thus considered the replacement of a F by an O associated with a Li vacancy next to it. The structure of the $Li_{15}V_{16}(PO_4)_{16}F_{15}O$ supercell was relaxed using GGA and GGA+U and the local electronic structure around the defect was analyzed. The two approaches lead to a similar picture. **Figure 9a** shows the calculated distances involving the two V ions around the O defect. They both now exhibit a short V-O bond (1.75 Å and 1.87 Å), but longer than in $LiVPO_4O$ (1.63 Å), since the same O is involved in the two V-O "vanadyl" type bonds. By analyzing the partial DOS, Bader charges and magnetization in a 0.64 Å radius sphere around V, it appears clearly that these two V ions are in the +IV state (S = ½) whereas the others remain +III (S = 1) (**Table S4**). However, they do not exhibit the same electronic spin configuration. **Figure 9b** shows the spin density maps around these V ions calculated in the $Li_{15}V_{16}(PO_4)_{16}F_{15}O$ cell. Whereas the V2' ions exhibit a similar electronic configuration to that of the V2' in the previous model (i.e. d_{xy}^1, with the lobe pointing toward a common edge between Li and V polyhedral), V1' exhibits a single occupied orbital that results from a recombination of the t_{2g} orbitals due to different local symmetry. The maximum spin density is thus located in lobes that no longer point through the common edge between Li and V polyhedra, but toward the center of the octahedron faces. Moreover, some V2'' of the first hypothesis now have no spin density in the d_{xy} orbital, recovering a normal spin density distribution. Here, 3 main different environments for Li can be described in the structure (**Figure 10)**. The Fermi contact shifts were again calculated for all the Li and are reported schematically in **Figure 11** below the experimental spectra. The Li_{LVPF}, Li_a and Li_b environments are similar to the ones previously described (**Figures 9a** and **9b**) and therefore the spin transfer mechanisms and calculated Fermi contact shifts (**Figure 11**) are similar to those of the first hypothesis, although they exhibit slightly different Li-O-V distances and angles leading to slightly different shifts. Li_c shares a common edge with V1' on the right side, with a different spin configuration than in the first hypothesis: V1' now

exhibits a single occupied orbital that results from a recombination of the t_{2g} orbitals due to different local symmetry. The resulting calculated Fermi contact shift is larger than for Li in $LiVPO_4F$ (Li_{LVPF} in **Figure 11)** and for Lia allowing the experimental signal assignment. However the precise spin mechanism from V1' to Li_c is not so clear.

Figure 11 shows a comparison between the calculated ^{7}Li NMR Fermi contact shifts for the 15 Li in the cell with the experimental ones. A correlation between experiment and theory can be made, proposing thus a complete assignment of the signals. We can correlate the entire defect signals in the experimental spectrum with the calculated ones; the most shifted experimental signal at 187 ppm is clearly split, which correlates well with the calculated shifts (Li_a and Li_c). The best correlation with experimental ^{7}Li NMR spectra was thus obtained with the second defect hypothesis, *i.e.* the local oxygen substitution for fluorine associated with a Li vacancy next to it.

In addition to the ^{7}Li NMR signals simulation, we calculated the ^{19}F NMR spectra and ^{31}P NMR spectra of $LiVPO_4F$, but only ^{7}Li NMR is relevant for the characterization of the defect. Indeed the ^{19}F NMR spectrum exhibits a large spinning sidebands manifold, which makes the identification of the isotropic signals not trivial, and overlapping with spinning sidebands is probable. For ^{31}P NMR, the signal is very broad, and thus possibly overlaps with the defect signal.

Conclusion

In the first part of this paper, we have validated the Fermi contact shifts calculations using the PAW approach as implemented in the VASP code. Using such a combined NMR/DFT approach permits to perform calculations on large supercells, and thus to consider the presence of defects in materials and their impact on the properties of these materials. Then, we applied this strategy by studying two types of possible defect in $LiVPO_4F$ leading to change of the Vanadium oxidation state. By analogy with the already existing $LiVOPO_4$ phase, we replaced one fluoride ion, along the chains of VO_2F_4, by an oxygen one. The best agreement between the calculated NMR spectra and the experimental one was achieved if a lithium vacancy is associated with the O defect, thus creating two V^{4+} ions around O. In each case, we analyzed the local electronic structure and the spin transfer mechanisms from V^{3+} or V^{4+} ions to the Li nuclei. Such combined NMR/DFT studies allow thus to understand defects in battery materials and their impact on the local electronic structure. Note that we are

presently working on $LiVPO_4F_{1-y}O_y$ materials and that confirm the choice of O-defect hypothesis in $LiVPO_4F$ (forthcoming paper).

Supporting Information

Additional information about the GGA calculation results, the Bader charge, and the calculated shifts obtained for other nuclei, and the geometrical optimization of $LiVPO_4F$. This material is available free of charge via the Internet at http://pubs.acs.org/.

Acknowledgments

The authors thank the French National Research Agency (STORE-EX Labex Project ANR-10-LABX-76-01 and HIPOLITE: Development of New High Voltage Positive Electrodes for Sustainable Li-Ion Batteries ANR-12-PRGE-0005-02), The Mésocentre de Calcul Intensif Aquitain (MCIA) and the modelling centre (ISM) are acknowledged for computing facilities. P. Aurel (ISM) is acknowledged for technical assistance.

References

(1) Masquelier, C.; Croguennec, L. Polyanionic (Phosphates, Silicates, Sulfates) Frameworks as Electrode Materials for Rechargeable Li (or Na) Batteries. *Chem. Rev.* **2013**, *113*, 6552–6591.

(2) Carlier, D.; Ménétrier, M.; Grey, C. P.; Delmas, C.; Ceder, G. Understanding the NMR Shifts in Paramagnetic Transition Metal Oxides Using Density Functional Theory Calculations. *Phys. Rev. B* **2003**, *67*, 174103.

(3) Castets, A.; Carlier, D.; Trad, K.; Delmas, C.; Ménétrier, M. Analysis of the 7Li NMR Signals in the Monoclinic Li3Fe2(PO4)3 and Li3V2(PO4)3 Phases. *J. Phys. Chem. C* **2010**, *114*, 19141–19150.

(4) Castets, A.; Carlier, D.; Zhang, Y.; Boucher, F.; Marx, N.; Croguennec, L.; Ménétrier, M. Multinuclear NMR and DFT Calculations on the LiFePO4·OH and FePO4·H2O Homeotypic Phases. *J. Phys. Chem. C* **2011**, *115*, 16234–16241.

(5) Mali, G.; Rangus, M.; Sirisopanaporn, C.; Dominko, R. Understanding 6Li MAS NMR Spectra of Li2MSiO4 Materials (M=Mn, Fe, Zn). *Solid State Nuclear Magnetic Resonance* **2012**, *42*, 33–41.

(6) Middlemiss, D. S.; Ilott, A. J.; Clément, R. J.; Strobridge, F. C.; Grey, C. P. Density Functional Theory-Based Bond Pathway Decompositions of Hyperfine Shifts: Equipping Solid-State NMR to Characterize Atomic Environments in Paramagnetic Materials. *Chem. Mater.* **2013**, *25*, 1723–1734.

(7) Seymour, I. D.; Middlemiss, D. S.; Halat, D. M.; Trease, N. M.; Pell, A. J.; Grey, C. P. Characterizing Oxygen Local Environments in Paramagnetic Battery Materials via 17O NMR and DFT Calculations. *J. Am. Chem. Soc.* **2016**, *138*, 9405–9408.

(8) Castets, A.; Carlier, D.; Zhang, Y.; Boucher, F.; Ménétrier, M. A DFT-Based Analysis of the NMR Fermi Contact Shifts in Tavorite-like LiMPO4·OH and MPO4·H2O (M = Fe, Mn, V). *J. Phys. Chem. C* **2012**, *116*, 18002–18014.

(9) Zhang, Y.; Castets, A.; Carlier, D.; Ménétrier, M.; Boucher, F. Simulation of NMR Fermi Contact Shifts for Lithium Battery Materials: The Need for an Efficient Hybrid Functional Approach. *J. Phys. Chem. C* **2012**, *116*, 17393–17402.
(10) Ellis, B. L.; Ramesh, T. N.; Davis, L. J. M.; Goward, G. R.; Nazar, L. F. Structure and Electrochemistry of Two-Electron Redox Couples in Lithium Metal Fluorophosphates Based on the Tavorite Structure. *Chem. Mater.* **2011**, *23*, 5138–5148.
(11) Nina V. Kosova, E. T. D. LiVPO4F/Li3V2(PO4)3 Nanostructured Composite Cathode Materials Prepared via Mechanochemical Way. *Journal of Solid State Electrochemistry* **2014**, *18*, 1389–1399.
(12) Cahill, L. S.; Chapman, R. P.; Britten, J. F.; Goward, G. R. 7Li NMR and Two-Dimensional Exchange Study of Lithium Dynamics in Monoclinic Li3V2(PO4)3. *J. Phys. Chem. B* **2006**, *110*, 7171–7177.
(13) Messinger, R. J.; Ménétrier, M.; Salager, E.; Boulineau, A.; Duttine, M.; Carlier, D.; Ateba Mba, J.-M.; Croguennec, L.; Masquelier, C.; Massiot, D.; Deschamps, M. Revealing Defects in Crystalline Lithium-Ion Battery Electrodes by Solid-State NMR: Applications to LiVPO4F. *Chem. Mater.* **2015**, *27*, 5212–5221.
(14) Ateba Mba, J.-M.; Masquelier, C.; Suard, E.; Croguennec, L. Synthesis and Crystallographic Study of Homeotypic LiVPO4F and LiVPO4O. *Chem. Mater.* **2012**, *24*, 1223–1234.
(15) Kresse, G.; Furthmüller, J. Efficiency of Ab-Initio Total Energy Calculations for Metals and Semiconductors Using a Plane-Wave Basis Set. *Computational Materials Science* **1996**, *6*, 15–50.
(16) Becke, A. D. A New Mixing of Hartree–Fock and Local Density-functional Theories. *The Journal of Chemical Physics* **1993**, *98*, 1372–1377.
(17) Tang, W.; Sanville, E.; Henkelman, G. A Grid-Based Bader Analysis Algorithm without Lattice Bias. *J Phys Condens Matter* **2009**, *21*, 084204.
(18) Sanville, E.; Kenny, S. D.; Smith, R.; Henkelman, G. Improved Grid-Based Algorithm for Bader Charge Allocation. *J Comput Chem* **2007**, *28*, 899–908.
(19) Graeme Henkelman, A. A. A Fast and Robust Algorithm for Bader Decomposition of Charge Density. *Computational Materials Science - COMPUT MATER SCI* **2006**, *36*, 354–360.
(20) Blöchl, P. E. First-Principles Calculations of Defects in Oxygen-Deficient Silica Exposed to Hydrogen. *Phys. Rev. B* **2000**, *62*, 6158–6179.
(21) Bianchini, M.; Ateba-Mba, J. M.; Dagault, P.; Bogdan, E.; Carlier, D.; Suard, E.; Masquelier, C.; Croguennec, L. Multiple Phases in the ε-VPO4O–LiVPO4O–Li2VPO4O System: A Combined Solid State Electrochemistry and Diffraction Structural Study. *J. Mater. Chem. A* **2014**, *2*, 10182–10192.
(22) Momma, K.; Izumi, F. *VESTA* : A Three-Dimensional Visualization System for Electronic and Structural Analysis. *Journal of Applied Crystallography* **2008**, *41*, 653–658.
(23) Boivin, E.; Chotard, J.-N.; Ménétrier, M.; Bourgeois, L.; Bamine, T.; Carlier, D.; Fauth, F.; Suard, E.; Masquelier, C.; Croguennec, L. Structural and Electrochemical Studies of a New Tavorite Composition: LiVPO4OH. *J. Mater. Chem. A* **2016**, *4*, 11030–11045.

Table captions

Table 1: Experimental ^{7}Li NMR shift compared to the calculated ones with GGA and GGA+U (U = 3.5 and 4.5eV) for $LiVPO_4F$.

Figure captions

Figure 1: Comparison between the experimental ^{7}Li Fermi contact shifts (ppm) and the calculated ones obtained for various compounds with the WIEN2k[4] and VASP codes using GGA and GGA+U approximations. a): for Tavorite materials ; b) : for anti-Nasicon materials

Figure 2: a) the $LiVPO_4F$ crystal structure[11] b) V-F distances in $LiVPO_4F$ c) LiO_4F local environment versus VO_4F_6 octahedra in the structure

Figure 3: ^{7}Li MAS NMR spectrum of $LiVPO_4F$ recorded at 116 MHz and 49.9 MHz (Hahn echo) using ν_r = 30 kHz spinning frequency. The spinning sidebands are marked with asterisks. An expanded area around the isotropic peaks is also shown.

Figure 4: a) 3D map of the spin density showing the spin transfer mechanism from the V to the Li in $LiVPO_4F$, visualized with VESTA and calculated with GGA+U approximation (U = 3.5 eV) for isosurface of 0.007 spin/Å^2. b) Schematic representation of the spin transfer mechanism from the transition metal to the Li nuclei.

Figure 5: Calculated V-O and V-F distances in $LiVPO_4F_{0.94}O_{0.06}$

Figure 6: 3D spin density map calculated for $LiVPO_4F_{0.94}O_{0.06}$ with GGA+U method (U eff = 3.5 eV) and an isosurface value equal to 0.007 spin/Å^2: yellow and blue surfaces indicate respectively positive and negative spin densities. a) 3D spin density in the whole cells, b) 3D spin density maps for the two V ions around the O defect, in comparison with the 3D spin density of $LiV^{IV}OPO_4$ given as inset of the right part showing the similarity between V2' and V ions in $LiV^{IV}OPO_4$.

Figure 7: 3D spin density map calculated for $LiVPO_4F_{0.94}O_{0.06}$ with GGA+U method (U eff = 3.5 eV) and an isosurface value equal to 0.007 spin/Å^2: yellow and blue surfaces indicate respectively positive and negative spin densities, showing 4 types of spin transfer mechanism. a) Li_a, b) Li_b, c) Li_c, and d) Li_d.

Figure 8: Comparison between the experimental ^{7}Li MAS NMR of $LiVPO_4F$ and the calculated one for the supercell with defect $LiVPO_4F_{0.94}O_{0.06}$

Figure 9: a) V-O and V-F distances in $Li_{0.94}VPO_4F_{0.94}O_{0.06}$; b) 3D spin density map of V2' and V1' around the O defect with GGA+U method (U eff = 3.5 eV) and an isosurface value equal to 0.007 spin/$Å^2$, yellow and blue surfaces indicate respectively positive and negative spin densities.

Figure 10: 3D spin density map calculated for $Li_{0.94}VPO_4F_{0.94}O_{0.06}$ with GGA+U method (Ueff = 3.5 eV) and an isosurface value equal to 0.007 spin/$Å^2$: yellow and blue surfaces indicate respectively positive and negative spin densities, showing 3 types of spin transfer mechanisms. a) Li_a, b) Li_b and c) Li_c.

Figure 11: Comparison between the experimental ^{7}Li MAS NMR signals of $LiVPO_4F$ and the calculated ones for the supercell with defect $Li_{0.94}VPO_4F_{0.94}O_{0.06}$

Table 1: Experimental ^{7}Li NMR shift compared to the calculated ones with GGA and GGA+U (U = 3.5 and 4.5eV) for $LiVPO_4F$.

	Exp. shifts (ppm)	Method	Calculated shifts (ppm)
^{7}Li	**116**	GGA	130
		GGA+U (U=3.5 eV)	121
		GGA+U (U=4.5 eV)	110

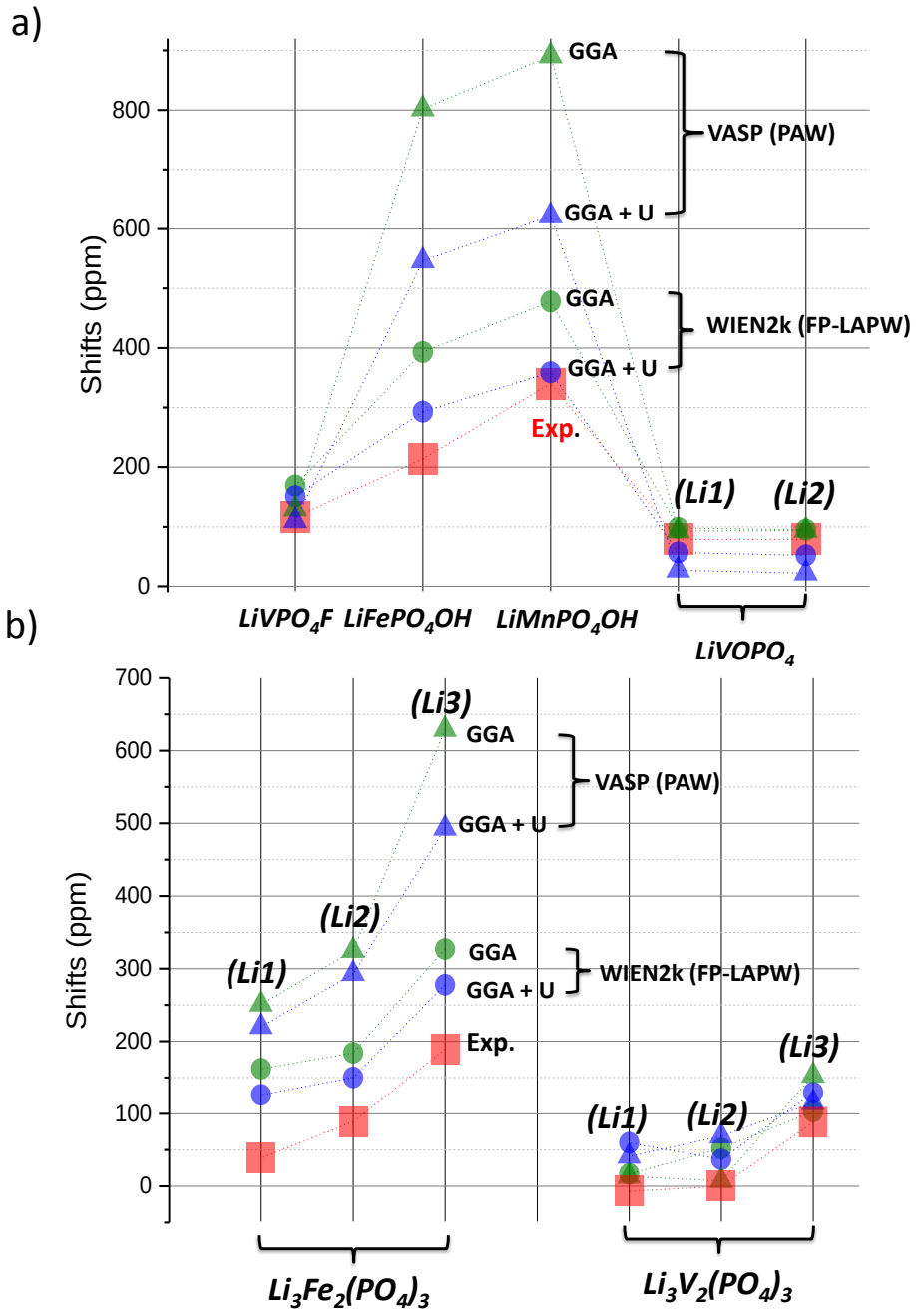

Figure 1: Comparison between the experimental ^{7}Li Fermi contact shifts (ppm) and the calculated ones obtained for various compounds with the WIEN2k[4] and VASP codes using GGA and GGA+U approximations. a): for Tavorite materials ; b) : for anti-Nasicon materials.

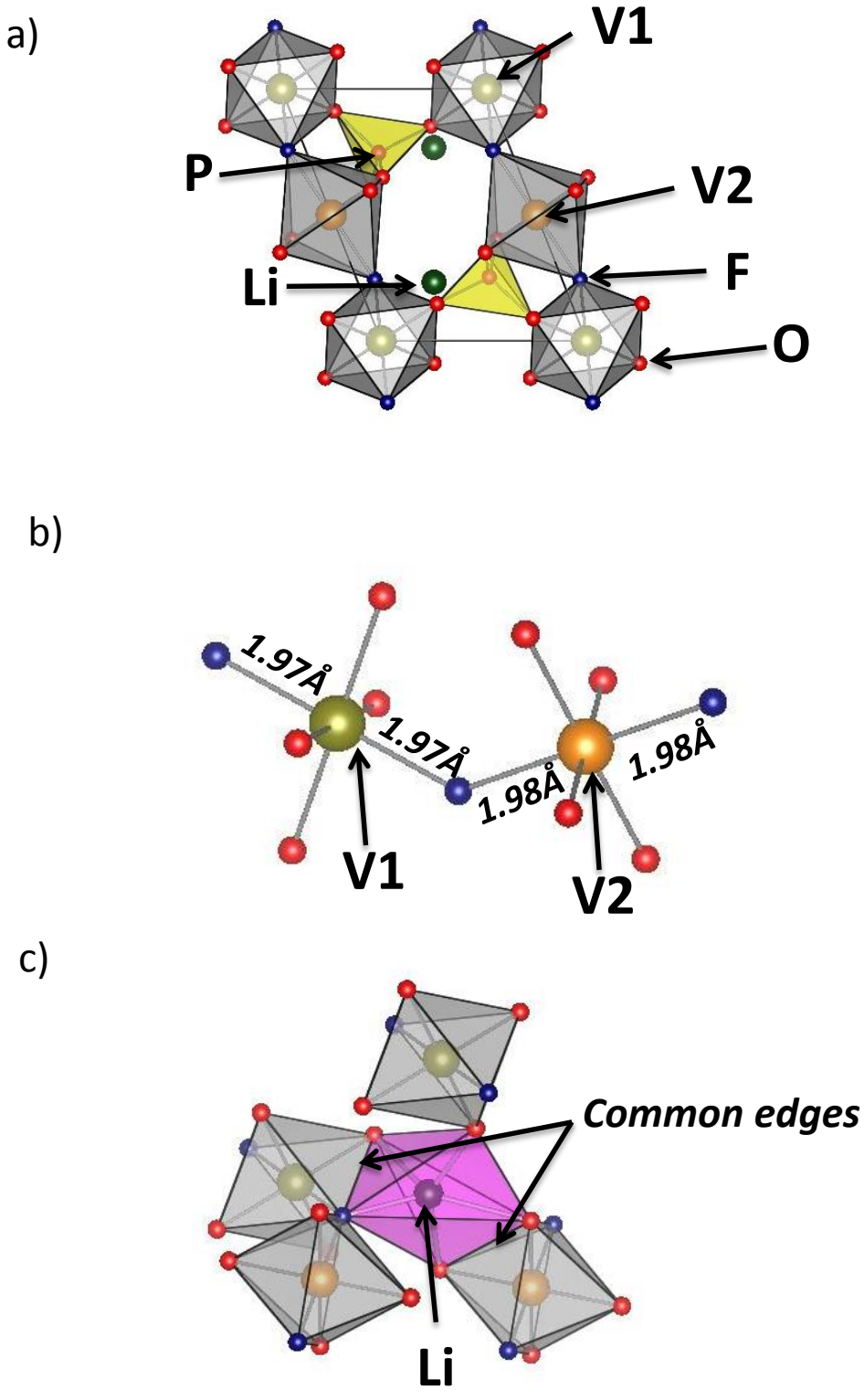

Figure 2: a) the $LiVPO_4F$ crystal structure[11] b) V-F distances in $LiVPO_4F$ c) LiO_4F local environment versus VO_4F_6 octahedra in the structure

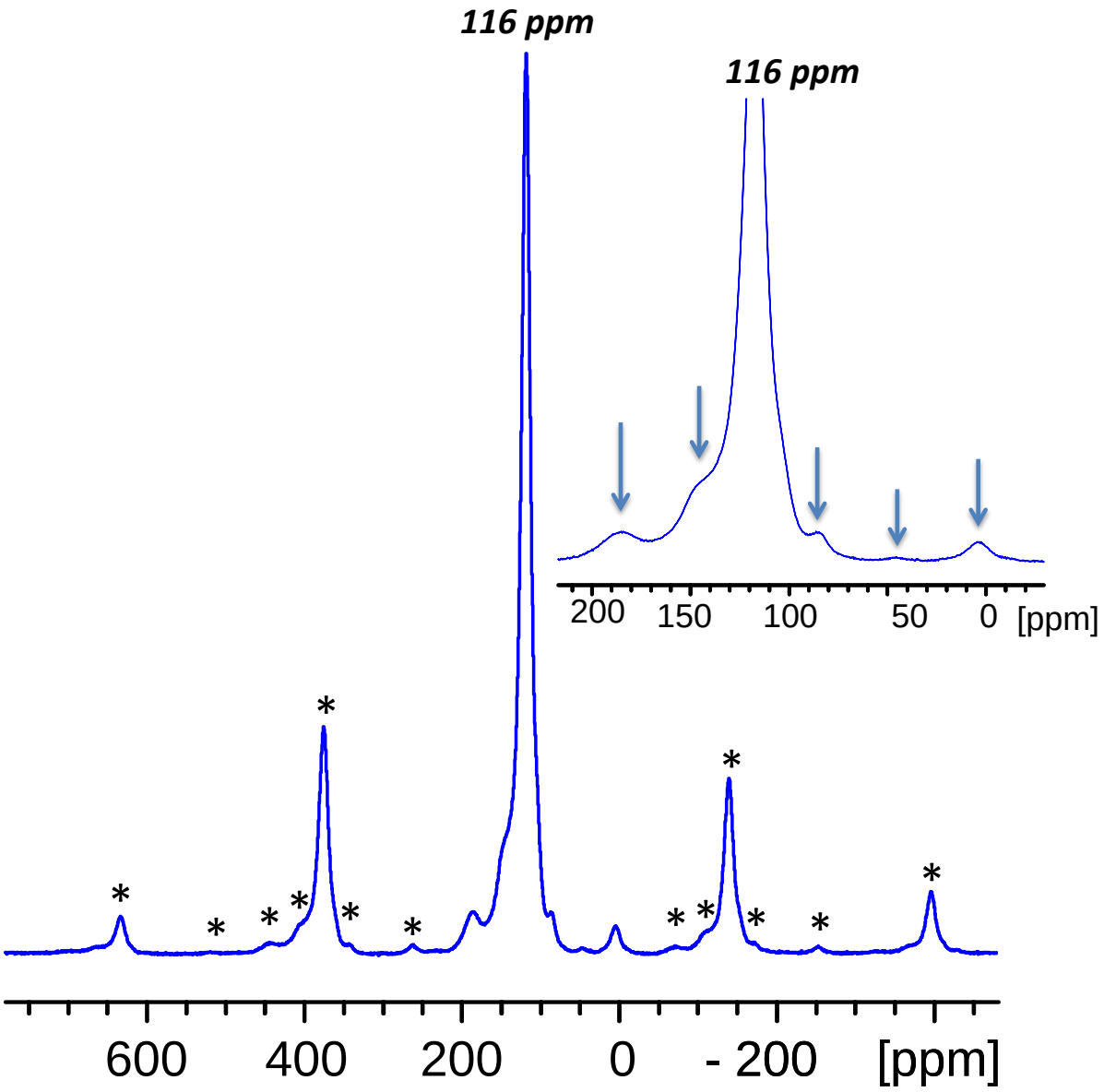

Figure 3: ^{7}Li MAS NMR spectrum of $LiVPO_4F$ recorded at 116 MHz Hahn echo) using ν_r = 30 kHz spinning frequency. The spinning sidebands are marked with asterisks. An expanded area around the isotropic peaks is also shown.

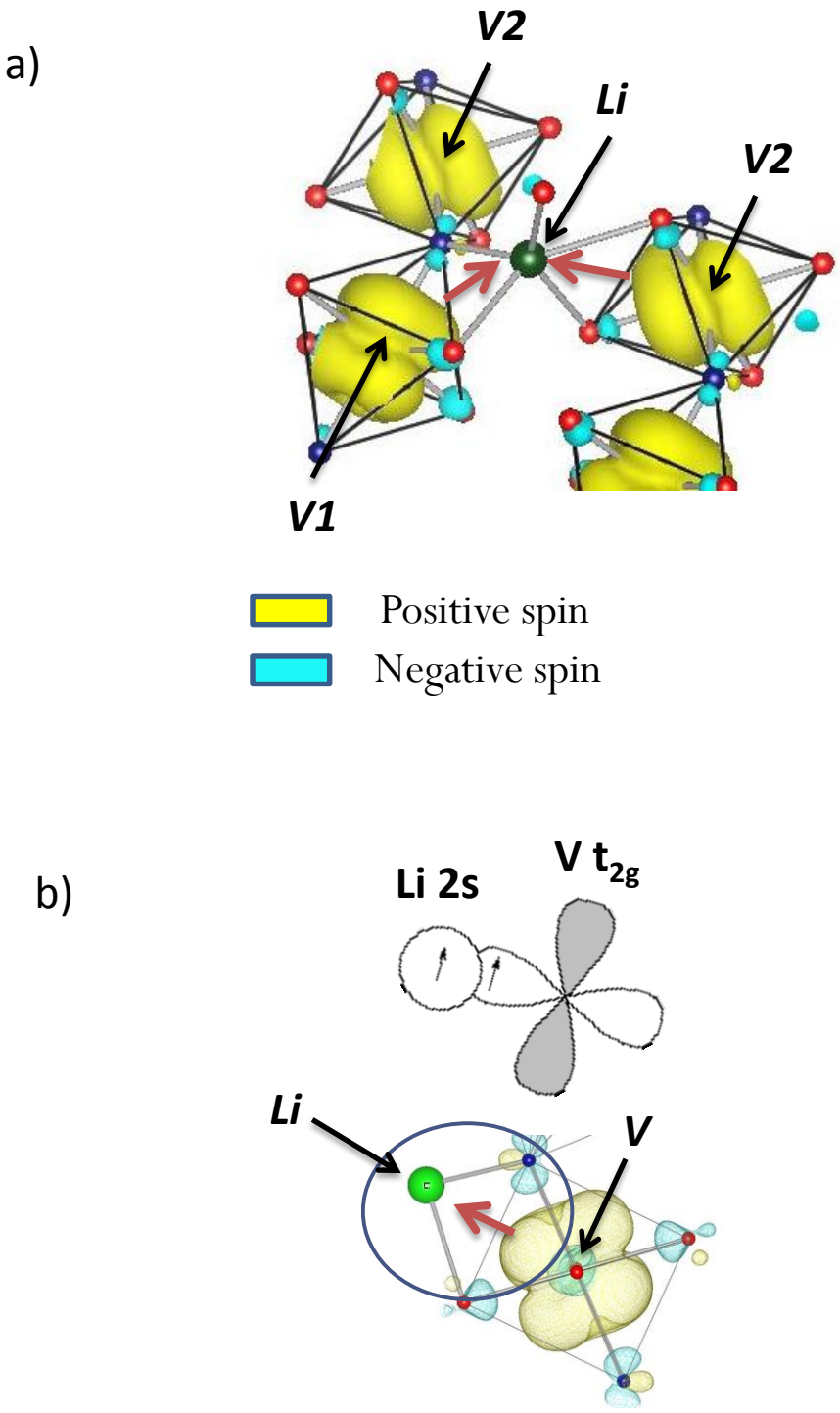

Figure 4: a) 3D map of the spin density showing the spin transfer mechanism from the V to the Li in $LiVPO_4F$, visualized with VESTA and calculated with GGA+U approximation (U = 3.5 eV) for isosurface of 0.007 spin/Å^2. b) 2D spin density map for V1 and schematic representation of the spin transfer mechanism from the transition metal to the Li nucleus.

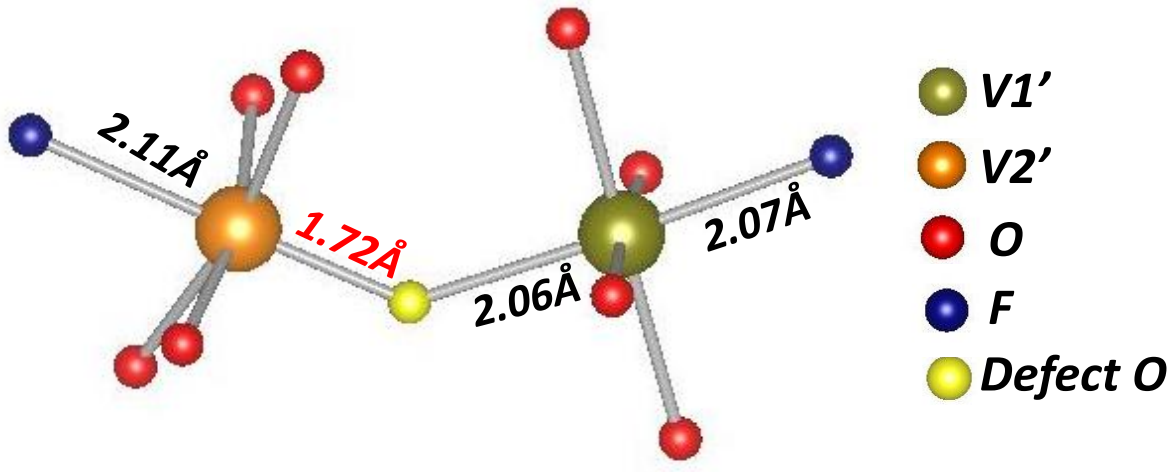

Figure 5: Calculated V-O and V-F distances in $LiVPO_4F_{0.94}O_{0.06}$

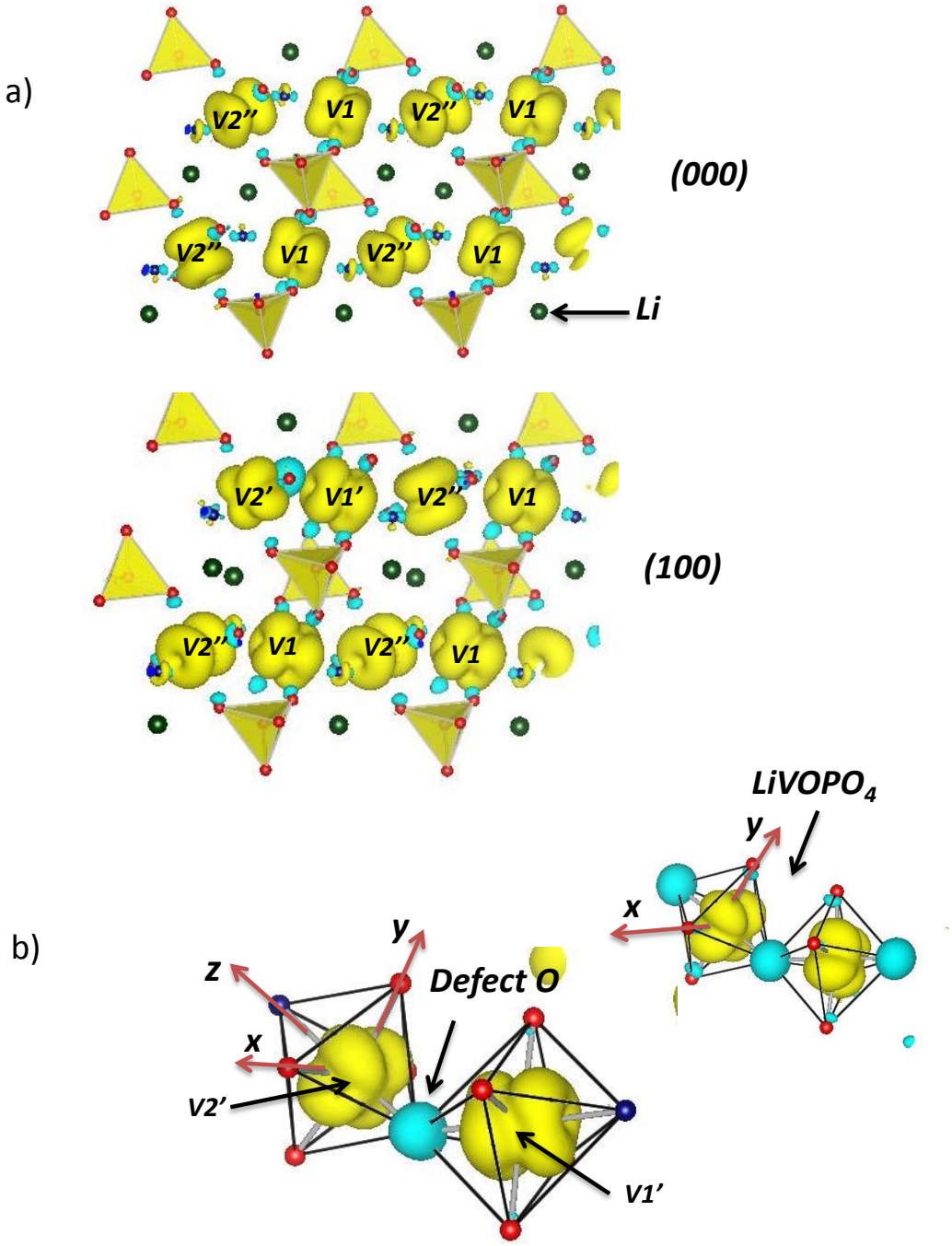

Figure 6: 3D spin density map calculated for $LiVPO_4F_{0.94}O_{0.06}$ with GGA+U method (U eff = 3.5 eV) and an isosurface value equal to 0.007 spin/Å^2: yellow and blue surfaces indicate respectively positive and negative spin densities. a) 3D spin density in the whole cells, b) 3D spin density maps for the two V ions around the O defect, in comparison with the 3D spin density of $LiV^{IV}OPO_4$ given as inset of the right part showing the similarity between V2' and V ions in $LiV^{IV}OPO_4$.

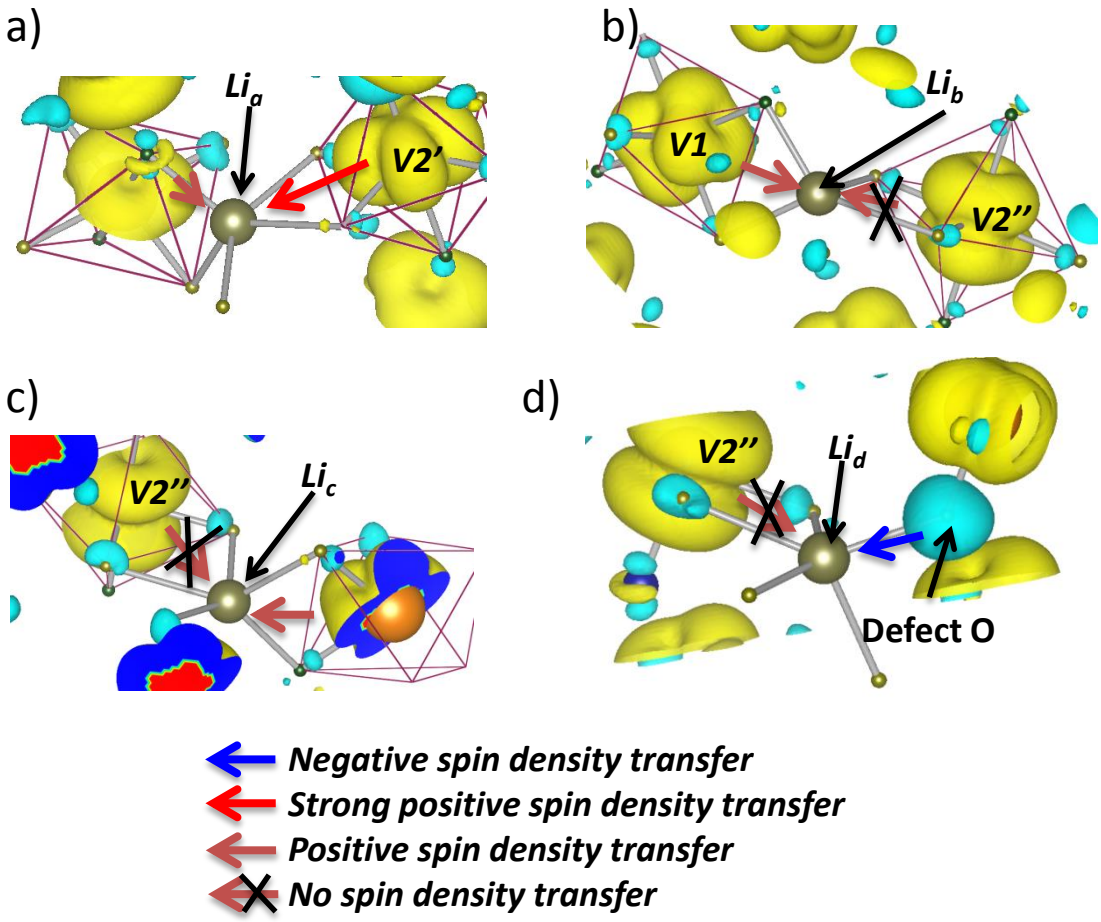

Figure 7: 3D spin density map calculated for $LiVPO_4F_{0.94}O_{0.06}$ with GGA+U method (U eff = 3.5 eV) and an isosurface value equal to 0.007 spin/Å^2: yellow and blue surfaces indicate respectively positive and negative spin densities, showing 4 types of spin transfer mechanism. a) Li_a, b) Li_b, c) Li_c, and d) Li_d.

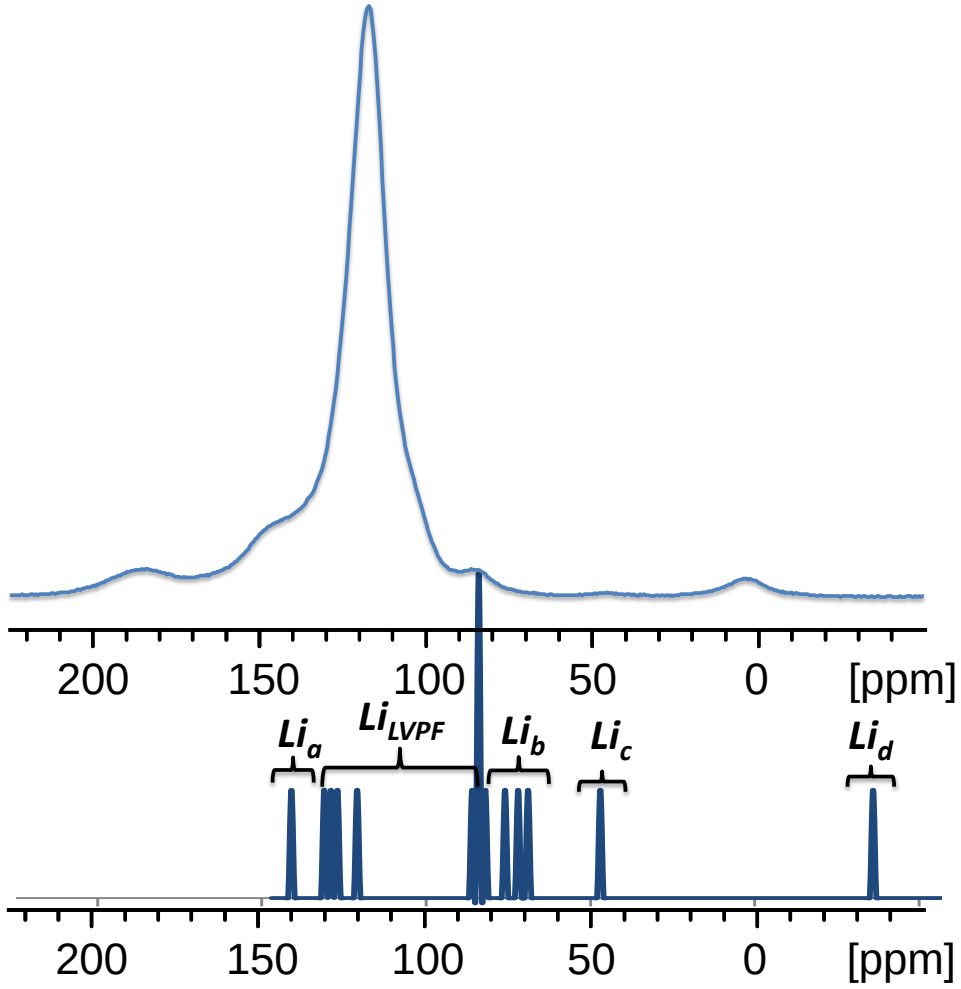

Figure 8: Comparison between the experimental ^{7}Li MAS NMR at 116 MHz of $LiVPO_4F$ and the calculated one for the supercell with defect $LiVPO_4F_{0.94}O_{0.06}$

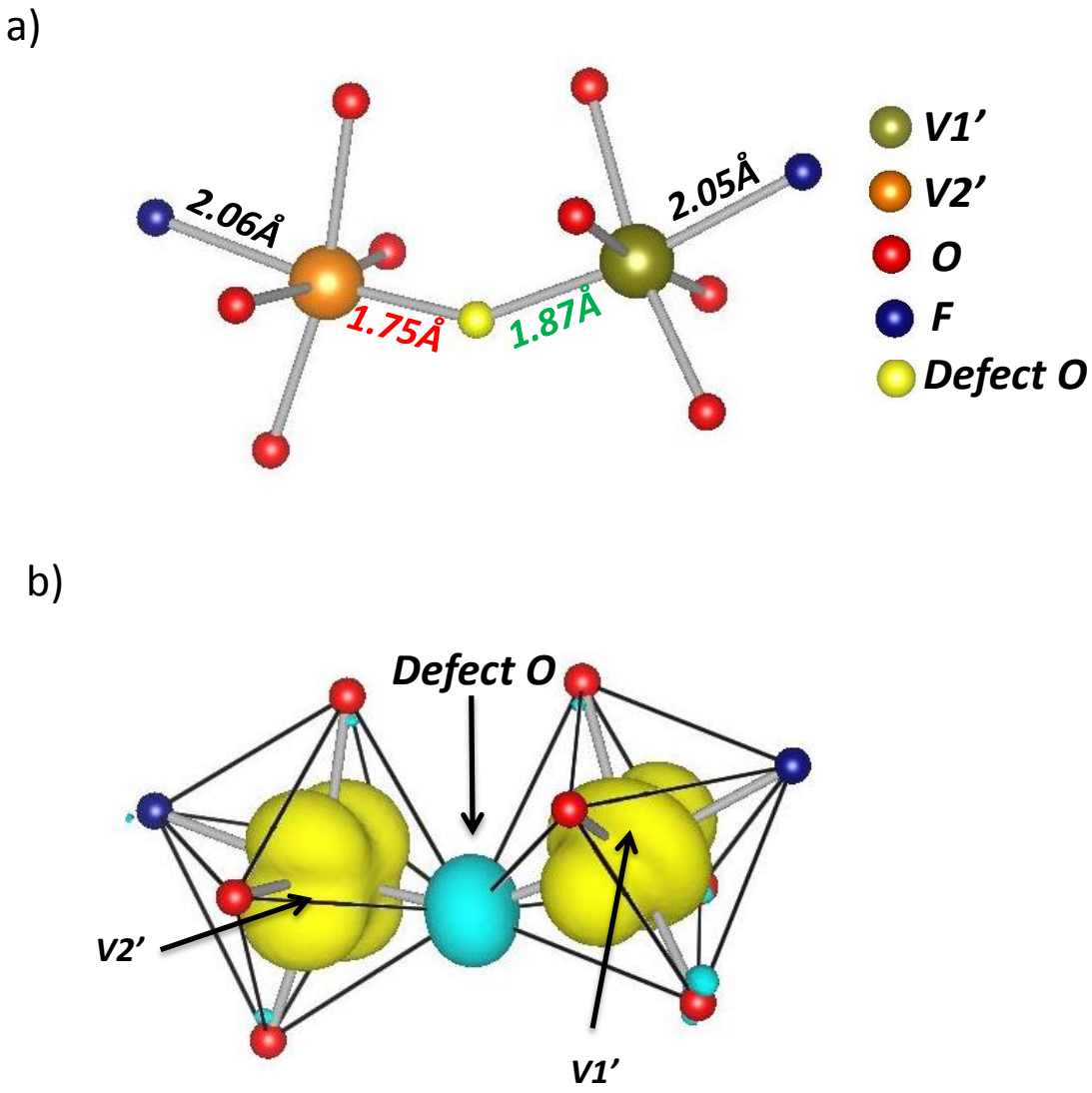

Figure 9: a) V-O and V-F distances in $Li_{0.94}VPO_4F_{0.94}O_{0.06}$; b) 3D spin density map of V2' and V1' around the O defect with GGA+U method (U eff = 3.5 eV) and an isosurface value equal to 0.007 spin/Å^2, yellow and blue surfaces indicate respectively positive and negative spin densities.

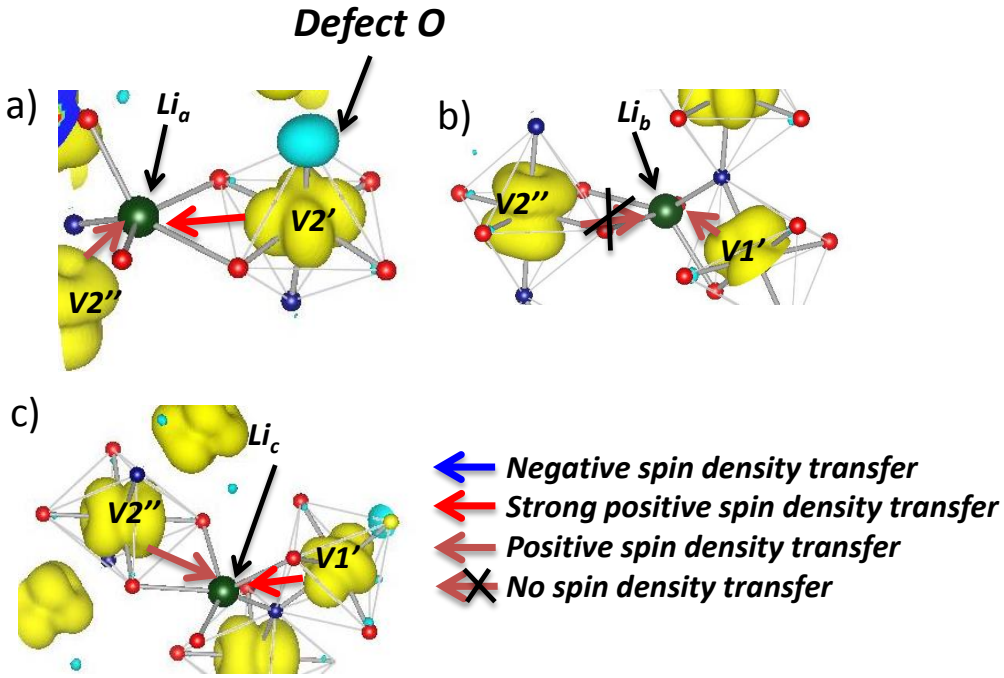

Figure 10: 3D spin density map calculated for $Li_{0.94}VPO_4F_{0.94}O_{0.06}$ with GGA+U method (Ueff = 3.5 eV) and an isosurface value equal to 0.007 spin/Å^2: yellow and blue surfaces indicate respectively positive and negative spin densities, showing 3 types of spin transfer mechanisms. a) Li_a, b) Li_b and c) Li_c.

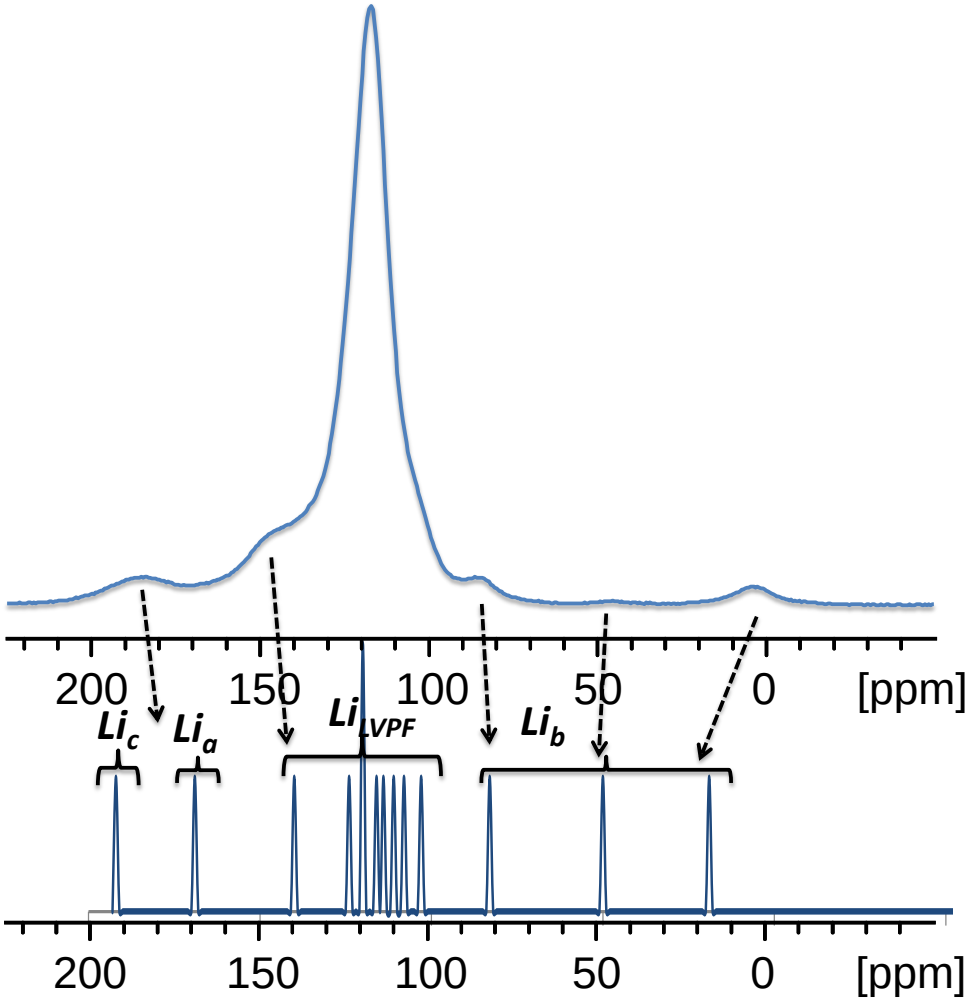

Figure 11: Comparison between the experimental ^{7}Li MAS NMR signals of $LiVPO_4F$ and the calculated ones for the supercell with defect $Li_{0.94}VPO_4F_{0.94}O_{0.06}$

Table of content (TOC)